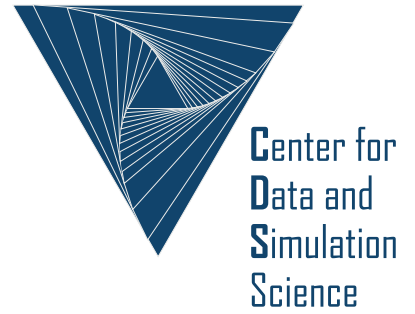


Universität
zu Köln



Technical Report Series Center for Data and Simulation Science

D. Balzani, A. Heinlein, A. Klawonn, O. Rheinbach, J. Schröder

Comparison of Arterial Wall Models in Fluid-Structure Interaction
Simulations

Technical Report ID: CDS-2022-01

Available at <http://kups.ub.uni-koeln.de/id/eprint/55586>

Submitted on March 04, 2022

Comparison of Arterial Wall Models in Fluid-Structure Interaction Simulations

D. Balzani¹, A. Heinlein², A. Klawonn^{3,4}, O. Rheinbach⁵, J. Schröder⁶ *

¹ Chair of Continuum Mechanics, Ruhr University Bochum, Bochum, Germany. daniel.balzani@rub.de

² Delft Institute of Applied Mathematics, Delft University of Technology, The Netherlands. a.heinlein@tudelft.nl

³ Department of Mathematics and Computer Science, University of Cologne, Weyertal 86-90, 50931 Köln, Germany, axel.klawonn@uni-koeln.de, <https://www.numerik.uni-koeln.de>.

⁴ Center for Data and Simulation Science, University of Cologne, Germany, <https://www.cds.uni-koeln.de>

⁵ Institut für Numerische Mathematik und Optimierung, Fakultät für Mathematik und Informatik, Technische Universität Freiberg, Akademiestr. 6, 09599 Freiberg, oliver.rheinbach@math.tu-freiberg.de, <https://www.mathe.tu-freiberg.de/nmo/mitarbeiter/oliver-rheinbach>

⁶ Institut für Mechanik, Fakultät für Ingenieurwissenschaften / Abtl. Bauwissenschaften, Universität Duisburg-Essen, 45141 Essen, Universitätsstr. 15, Germany, j.schroeder@uni-due.de

Received: date / Revised version: date

Abstract Monolithic fluid-structure interaction (FSI) of blood flow with arterial walls is considered, making use of sophisticated nonlinear wall models. These incorporate the effects of almost incompressibility as well as of the anisotropy caused by embedded collagen fibers. In the literature, relatively simple structural models such as Neo-Hooke are often considered for FSI with arterial walls. Such models lack, both, anisotropy and incompressibility.

In this paper, numerical simulations of idealized heart beats in a curved benchmark geometry, using simple and sophisticated arterial wall models, are compared: we consider three different almost incompressible, anisotropic arterial wall models as a reference and, for comparison, a simple, isotropic Neo-Hooke model using four different parameter sets.

The simulations show significant quantitative and qualitative differences in the stresses and displacements as well as the lumen cross sections. For the

* *Present address:* Insert the address here if needed

Coupling Algorithm	Time for one time step			GMRES iter		
	1 CPU	2 CPUs	4 CPUs	1 CPU	2 CPUs	4 CPUs
Dirichlet-Neumann	31 s	26 s	22 s	15	15	15
Neumann-Dirichlet	866 s	729 s	635 s	567	567	567
Neumann-Neumann ($\alpha_s = 0.5, \alpha_f = 0.5$)	590 s	501 s	434 s	274	274	274
Neumann-Neumann ($\alpha_s = 0.999, \alpha_f = 0.001$)	40 s	34 s	30 s	20	21	21
Neumann-Neumann ($\alpha_s = 0.9999, \alpha_f = 0.0001$)	32 s	28 s	24 s	15	15	15
Monolithic Dirichlet-Neumann	12 s	8 s	5 s	11	25	50

Table 1.1 A comparison of different Steklov-Poincaré fluid-structure interaction algorithms, that is, Dirichlet-Neumann, Neumann-Dirichlet, Neumann-Neumann (using different scaling factors), and the monolithic Dirichlet-Neumann preconditioner (composed GCE [14]). A parallel overlapping Schwarz preconditioner is used for the blocks where the number of subdomains is identical to the number of CPUs. For the monolithic Dirichlet-Neumann preconditioner the number of GMRES iteration grows since the inverse in the block is replaced by a one-level overlapping Schwarz preconditioner. Nonetheless, the monolithic scheme is faster and shows a better scalability. Results from [17, Table 1].

Neo-Hooke models, a significantly larger amplitude in the in- and outflow areas during the heart beat is observed, presumably due to the lack of fiber stiffening. For completeness, we also consider a linear elastic wall using 16 different parameter sets. However, using our benchmark setup, we were not successful in achieving good agreement with our nonlinear reference calculation.

1 Introduction

We are interested in fluid-structure interaction (FSI) problems in biomechanics, notably the interaction of blood flow with arterial walls. In hemodynamics the densities of the fluid and the structure are similar, that is, $\rho_f \approx \rho_s$, and the structure is soft, compared to other FSI applications, for instance, in aeroelasticity. In this regime, strong FSI coupling schemes are most suitable, and monolithic FSI coupling schemes have been demonstrated to be most competitive; see, e.g., [6, 16, 30, 29, 13, 33, 37, 18, 28, 12, 20].

In [17], we have compared, in the context of hemodynamics, different segregated strong coupling schemes based on Steklov-Poincaré formulation of the FSI problem [15]. We have considered Dirichlet-Neumann, Neumann-Dirichlet, Neumann-Neumann (using different scalings) and a monolithic approach, that is, the composed Dirichlet-Neumann preconditioner [13]. The monolithic approach [13] was significantly faster, by a factor of two to four, than the fastest segregated approach (segregated Dirichlet-Neumann) and showed a better parallel scalability [17, Table 1]; see also Table 1.1.

Here, the Dirichlet-Neumann algorithms refer to using $S'_s{}^{-1}$, the inverse of the structure tangent, as a preconditioner for $S'_f + S'_s$, the sum of the tangents of the fluid and structure Steklov-Poincaré operators. The

segregated Dirichlet-Neumann method [15], the scaled Neumann-Neumann method [17], and the monolithic Dirichlet-Neumann method [13] are closely related, and the performance will be very similar if exact solvers are used for the tangent problems. Therefore, the performance benefit of the monolithic method comes from the use of inexact solvers for the blocks.

Our focus is on the application of sophisticated structural models for the arterial wall since we are interested in quantities inside the arterial wall, such as the transmural stresses, which are associated with atherogenesis, that is, the narrowing of arteries due to plaque formation. Note that by *sophisticated structural models* we refer to geometrically and physically nonlinear, hyperelastic, and anisotropic models since the main interest here is the analysis of the blood-wall interaction under physiological conditions. If supra-physiological loadings are to be analyzed, for example, resulting from balloon-angioplasty, then even more complex models describing the stress-softening response associated with microscopic damage need to be applied; see e.g. [5,9]).

The state of the art in the hyperelastic modeling of the passive response of arterial wall tissue considers (almost) incompressibility and also anisotropy from stiffening collagen fibers. The resulting problems are already difficult to solve iteratively without FSI, that is, as a structural mechanics problem alone [11,21]. It was then shown in [7,6] that FSI simulations with such challenging structural models are feasible. It is known from experiments that arterial walls show some visco-elastic behavior; we therefore have also considered visco-elastic effects in our FSI simulations [7,6]. However, it was already concluded in [7] that the influence of viscoelasticity on our quantities of interest, for example, the wall shear stresses, is rather small. Therefore, we usually focus on almost incompressible, anisotropic hyperelastic models without viscoelasticity.

However, since much simpler models for the structure are often used in hemodynamics, it is of interest to investigate the structural model's influence on the simulation results. Our FSI simulations in [23] have already indicated that sophisticated structural models, such as the model denoted Ψ_A in [10,3,6] (originally introduced in [8]), result in a qualitatively different deformation of the wall compared to Neo-Hooke or linear elasticity [23, Section 6.3 and Fig. 18]. We also showed in numerical tests that, even for the relatively small time steps necessary in our context, adding a coarse level to an overlapping Schwarz preconditioner [23, Fig. 19] will accelerate the convergence. In this paper, we now investigate in more detail how the response of simpler structural models, such as Neo-Hooke, is different from the results obtained with more sophisticated models, which incorporate the almost incompressibility of biological soft tissue as well as the anisotropy from stiffening collagen fibers in the arterial wall.

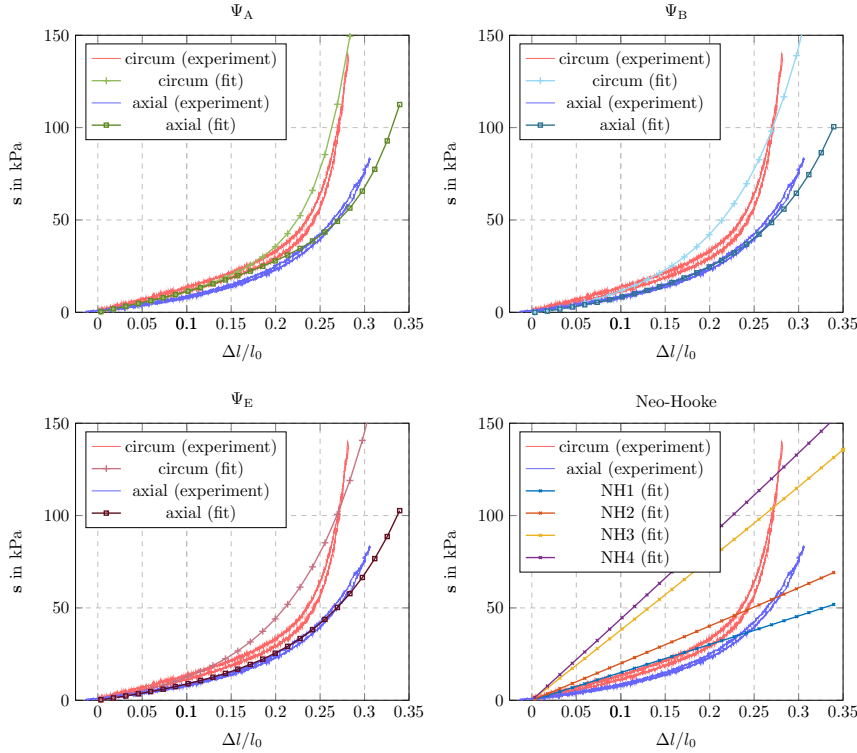


Fig. 2.1 Stress-strain plots for the experimental data and the different material models. A good fit can not be achieved using the Neo-Hooke material model, however, NH1 yields a sufficient fit for the $\Delta l/l_0 < 0.2$.

2 Arterial wall models

Let $\mathbf{F} := \nabla\varphi$ be the deformation gradient mapping infinitesimal vectorial elements in the reference configuration onto the current configuration. The mapping of infinitesimal volume elements is then described by $J := \det \mathbf{F}$. In order to automatically fulfill the principle of objectivity, we consider models formulated in the right Cauchy-Green deformation tensor $\mathbf{C} := \mathbf{F}^T \mathbf{F}$. For hyperelastic materials, a strain energy density function Ψ as a function of the deformation tensor is defined. In order to guarantee a physically reasonable material response avoiding a loss of material stability [35], here, polyconvex energy functions in the sense of [2] will be considered. By evaluation of the second law of thermodynamics, the 2nd Piola-Kirchhoff stress tensor and the Cauchy stress tensor can be computed by

$$\mathbf{S} = 2 \frac{\partial \Psi}{\partial \mathbf{C}} \quad \text{and} \quad \boldsymbol{\sigma} = J^{-1} \mathbf{F} \mathbf{S} \mathbf{F}^T,$$

respectively. Based on the Cauchy stress tensor, the von Mises stresses can be computed. For a convenient construction of suitable strain energy den-

sity functions, often the invariants of the functional arguments in the energy function are considered. For isotropic materials, the principle invariants of \mathbf{C} , that is,

$$I_1 = \text{tr } \mathbf{C}, \quad I_2 = \text{tr}[\text{Cof}(\mathbf{C})], \quad I_3 = \det \mathbf{C},$$

with $\text{Cof}(\mathbf{C}) = \det(\mathbf{C})\mathbf{C}^{-T}$, are taken into account and thus, $\Psi := \Psi(I_1, I_2, I_3)$. Note that in the context of soft biological tissues, often the dependence on the second invariant is omitted. Thereby, the material response is mainly governed by normal stretches described through I_1 and volume changes described by $I_3 = (\det \mathbf{F})^2$. As a result of embedded collagen fibers, arterial wall tissues behave anisotropically. The fibers are wound crosswise helically around the artery and in healthy arteries symmetrically disposed with respect to the axial direction. Assuming a weak interaction between the fiber families, the resulting anisotropy can be modelled by superimposing two transversely isotropic models. For the individual fiber family and thus, the description of transverse isotropy, the structural tensor $\mathbf{M} = \mathbf{a} \otimes \mathbf{a}$, $\|\mathbf{M}\| = 1$ [36] is considered as additional argument in the strain energy density function. Herein, the preferred direction vector \mathbf{a} describes the fiber orientation. Thus, for a coordinate-invariant formulation, the mixed invariants

$$J_4 = \text{tr}[\mathbf{C}\mathbf{M}], \quad J_5 = \text{tr}[\mathbf{C}^2\mathbf{M}],$$

are taken into account. Whereas J_4 describes the square of the stretch in fiber direction \mathbf{a} , the physical meaning of J_5 is unclear.

2.1 Simple, isotropic material model: Neo-Hooke

As a simple, isotropic nonlinear material model, we consider a standard compressible Neo-Hookean energy. It is often written in the form

$$\Psi_{\text{NH}} = \Psi_{\text{vol}} + \Psi_{\text{isoch}},$$

where the volumetric and isochoric parts are given by

$$\Psi_{\text{vol}} = \frac{\kappa}{2} (\ln(I_3^{1/2}))^2 \quad \text{and} \quad \Psi_{\text{isoch}} = \frac{\mu}{2} (I_3^{-1/3} I_1 - 3).$$

The material parameters are κ and μ and modulate an increase of energy related to a volume change and a change of isochoric deformations, respectively. Due to the fact that soft biological tissues are mostly assumed to be almost incompressible, here, the volumetric energy will be used as a penalty function to adjust for the quasi-incompressibility constraint. Since the stresses are obtained as derivatives of the energy functions with respect to the deformation tensor, an increase of μ thus corresponds to an increase in stiffness and for incompressibility mainly modulates the slope in stress-strain diagrams of uniaxial tension tests. Since the Neo-Hookean model is not able to catch the stiffening of the tissue caused by the collagen fibers,

Parameter set	κ in kPa	μ in kPa
NH ₁	2 500.0	50.4
NH ₂	3 333.3	67.1
NH ₃	6 333.3	127.52
NH ₄	7 333.3	147.65

Table 2.1 Material parameter sets for the Neo-Hooke model. Higher indices correspond to a higher stiffness.

the parameters were fitted by hand to the experiments in [25]; see also [8]. There, uniaxial tension tests were performed in circumferential and axial direction of human artery segments. Whereas the parameter set NH₁ was fitted to approximate the slope of the experimental curves (media) in the range $0 < \Delta l/l_o < 0.2$, the set NH₂ approximately corresponds to the average slope of the experimental curve in the range $0 < \Delta l/l_o < 0.235$ and thus, results in a slightly stiffer behavior. NH₃ and NH₄ were chosen significantly stiffer in order to obtain a similar lumen area as the anisotropic models before the start of the heart beat; see also section 4.1. The parameter sets are summarized in Table 2.1.

The resulting stress-stretch curves are compared with the experiments in Figure 2.1. Note that the experimental data shows a slight hysteresis resulting from a negligible visco-elastic response. We will see in the FSI simulations in section 4 that, for NH₁ and NH₂, the resulting material behavior is significantly softer compared to the sophisticated, anisotropic models; see Figure 4.2.

For the sets NH₃ und NH₄ the in- and outflow lumen in the simulations presented later is, at the end of the ramp, similar to the lumen areas of the sophisticated models. These parameter sets correspond well for a specific loading scenario in a structural problem, but due to their artificially stiff response, the associated stress-strain curves will not match well the experimental curves on average. For all parameter sets, the compression modulus κ was chosen such that the volume change of the model response was kept below 1% in the uniaxial tension tests.

Note that, in the benchmark computations presented in [6, Figure 21], based on the material model Ψ_A , the increase of the arterial circumference during the heartbeat was below 20%.

2.2 Anisotropic material models

Following the analysis in [10], we consider different anisotropic and quasi-incompressible material models for arterial walls. They are of the form

$$\Psi_X = \Psi_{X,\text{iso}}(I_1, I_3) + \sum_{a=1}^2 \Psi_{X,(a)}^{\text{ti}}(I_1, I_3, J_4^{(a)}, J_5^{(a)})$$

where $X \in \{A, B, E\}$. Herein, the mixed invariants are considered separately for the two fiber family directions $\mathbf{a}^{(a)}$, $a = 1, 2$, i.e., $J_4^{(a)} = \text{tr}(\mathbf{C}\mathbf{M}^{(a)})$ and $J_5^{(a)} = \text{tr}(\mathbf{C}^2\mathbf{M}^{(a)})$ with $\mathbf{M}^{(a)} = \mathbf{a}^{(a)} \otimes \mathbf{a}^{(a)}$. In detail, the individual functions are

Model Ψ_A [8]

$$\begin{aligned}\Psi_{A,\text{iso}}(I_1, I_3) &= \epsilon_1(I_3^{\epsilon_2} + I_3^{-\epsilon_2} - 2) + c_1(I_1 I_3^{-1/3} - 3), \\ \Psi_{A,(a)}^{\text{ti}}(I_1, J_4^{(a)}, J_5^{(a)}) &= \alpha_1 \left\langle I_1 J_4^{(a)} - J_5^{(a)} - 2 \right\rangle^{\alpha_2},\end{aligned}$$

Model Ψ_B (isochoric and anisotropic part from [26])

$$\begin{aligned}\Psi_{B,\text{iso}}(I_1, I_3) &= \epsilon_1(I_3^{\epsilon_2} + I_3^{-\epsilon_2} - 2) + c_1(I_1 I_3^{-1/3} - 3), \\ \Psi_{B,(a)}^{\text{ti}}(I_3, J_4^{(a)}) &= \frac{k_1}{2k_2} \left(\exp \left(k_2 \left\langle J_4^{(a)} I_3^{-1/3} - 1 \right\rangle^2 \right) - 1 \right),\end{aligned}$$

Model Ψ_E (anisotropic part from [27])

$$\begin{aligned}\Psi_{E,\text{iso}}(I_1, I_3) &= \epsilon_1(I_3^{\epsilon_2} + I_3^{-\epsilon_2} - 2) + c_1(I_1 - 3 - \ln(I_3)), \\ \Psi_{E,(a)}^{\text{ti}}(J_4^{(a)}) &= \frac{k_1}{2k_2} \left(\exp \left(k_2 \left\langle J_4^{(a)} - 1 \right\rangle^2 \right) - 1 \right).\end{aligned}$$

Herein, the Macauley brackets $\langle \langle \bullet \rangle \rangle := ((\bullet) - |(\bullet)|)/2$ filter out negative values. Note that $\Psi_{A,\text{iso}} = \Psi_{B,\text{iso}}$. The models Ψ_B and Ψ_E are based on the well-known Holzapfel, Gasser, and Ogden model, where the transversely isotropic parts do not include I_1 and J_5 . They are formulated such that a specifically stiff response is purely generated in the fiber directions. In contrast to this, the model Ψ_A includes J_5 and even a coupling of I_1 with J_4 . Although J_5 may not directly have a physical meaning, the term $I_1 J_4 - J_5$ as part of Ψ_A was found in [34] to describe the change of infinitesimal area elements with normal vectors perpendicular to the fiber direction. Due to the coupling term $I_1 J_4$ in this model, a somewhat dispersed stiffness around the fiber direction is also included. Only the model Ψ_B is formulated in a volumetric-isochoric split. Whereas this may enable a more direct quantitative interpretation of the material parameters, it also renders the model response questionable under purely volumetric loading since the stress response will then be purely isotropic. In addition to that, the uncontrolled volume change in the isochoric energy may be problematic in finite element formulations where, for example, the volume change is only considered as volume average of each finite element, or associated terms are used for reduced integration. Summarizing, all models are quasi-incompressible, provided that sufficiently large parameters in the volumetric penalty functions are considered, they are highly nonlinear, anisotropic, polyconvex, and widely used, but each of them has certain advantages and disadvantages. We use the parameters for the media fitted in [10, Figure 2] to the experiments

performed in [25] which are given in Table 2.2. Note that the parameters used here for Ψ_A correspond to Ψ_A Set 2 in [10] and are identical to the parameters used for Ψ_A in [6]. Although the models Ψ_A and Ψ_B have the same isotropic part $\Psi_{*,\text{iso}}$, the parameters for $\Psi_{*,\text{iso}}$ are not the same.

Model	c_1 in kPa	ϵ_1 in kPa	ϵ_2	α_1 in kPa	α_2	k_1 in kPa	k_2
Ψ_A	17.5	499.8	2.4	30 001.9	5.1	-	-
Ψ_B	10.7	207.1	9.7	-	-	1 018.8	20.0
Ψ_E	9.7	95.3	3.8	-	-	687.6	20.0

Table 2.2 Material parameter sets for nonlinear, anisotropic models. The parameters for Ψ_A correspond to Ψ_A Set 2 in [10].

Note that all parameters for the simple isotropic and the sophisticated anisotropic models were obtained from adjusting to uniaxial tension tests which correspond to extreme values of stress ratios of circumferential to axial stresses ranging from 0 to infinity, which are often found difficult, already for engineering materials [31]. In real arteries, however, a uniaxial stress scenario cannot be expected and rather biaxial stress scenarios appear with stress ratios of moderate intensity in between the extreme values. Therefore, in principle, it would be advantageous to also include biaxial test data, but these are in turn difficult to obtain for soft biological tissues and their accuracy should be considered critically, especially for experiments performed on individual layers like the media and adventitia of small arteries. Uniaxial tests may therefore be considered more reliable, but a perfect match of the models with the experimental data should not be overrated. Therefore, the somewhat better agreement of model Ψ_A with the nonlinear experimental stress-strain response (cf. Figure 2.1) should not be given too much importance.

3 The curved tube fluid-structure benchmark problem

Although the final goal is the simulation of patient-specific arteries [4], the systematic, comparable analysis of numerical schemes is enhanced by concentrating on standardized boundary value problems. Therefore, we make use of the benchmark problem introduced in [6], a curved tube with an elastic wall; the inner radius of the tube is 0.15 cm, the outer radius is 0.21 cm, the radius of the curvature is 1 cm and the length of the straight part towards the outflow is also 1 cm; see [6, Figure 1] and also our figures in section 4. As a result, the in- and outflow areas are approximately 0.0707 cm² at the start of our simulations.

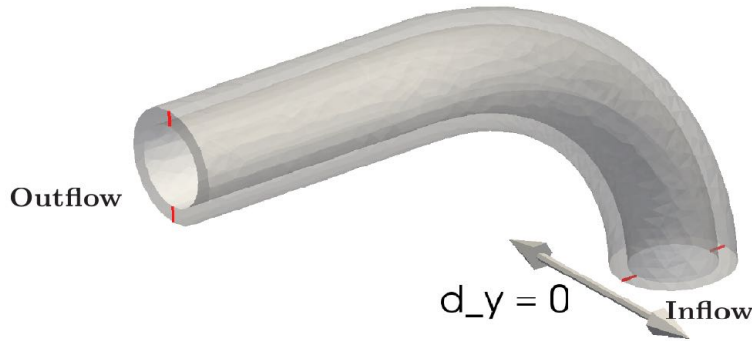


Fig. 3.1 At the red nodes the displacement is fixed y-direction. Image taken from [6] (copyright Wiley).

3.1 Mesh

We use a tetrahedral mesh with matching fluid and solid nodes at the interface. The mesh has 66 648 degrees of freedom for \mathbf{u} , 3 515 d.o.f. for p , 425 700 d.o.f. for \mathbf{d}_s , 28 044 d.o.f. for λ , and 66 648 d.o.f. for \mathbf{d}_f . In particular, we use Mesh #3 in [6, Table 6], where mesh convergence has been observed [6, Figure 21 and Figure 44] for \bar{F} finite elements.

3.2 Boundary conditions

The displacement of the structure is fixed in axial direction at the faces at both ends of the tube as well as at the red nodes in Figure 3.1. Combining these boundary conditions, we obtain a statically determined structure.

As in [6], we use an absorbing boundary condition [32] at the outlet in order to reduce wave reflections. Note that these absorbing boundary conditions are based on a one-dimensional model for the fluid and a simple linear model for the structure, that is, it uses a simple relation between the outflow area A and the pressure P ,

$$P = \frac{\beta}{\pi} \left(\sqrt{A} - \sqrt{A_0} \right),$$

where A_0 is the area at $t = 0$, and β is a parameter. In our nonlinear setting, this absorbing boundary condition will not remove reflections completely. Note that we have chosen β as in [6], such that it corresponds to a Young modulus of 120 kPa and a Poisson ratio of 0.49. We have used these values for all numerical experiments, that is, for all material models and all parameter sets. It is clear that for parameter sets corresponding to a significantly different stiffness of the structure the value of β will not be suitable to remove wave reflections, and some difficulties in our simulations may be due to this effect; see section 4.

4 Numerical results

In our numerical experiments, we consider the fluid structure interaction of fluid flow in the curved tube benchmark geometry defined in [6]. The benchmark in [6] was computed using Ψ_A with the same parameters as here; see section 2.2 for all material parameters.

The geometry consists of a curved and a straight section and can be seen as an idealized coronary artery; in particular, it corresponds only to the media, neglecting the intima and adventitia of the arterial wall. The tube is composed of a single material, that is, we use the nonlinear hyperelastic material models described in section 2 and the corresponding parameters. The fiber angle is set to $\beta_f = 43$ degrees. As the spatial discretization, we use P_2 - P_1 (Taylor-Hood) finite elements for the fluid and P_2 elements for the geometry problem. For the structure, we use either P_2 elements for the linear elastic or Neo-Hooke wall models or \bar{F} finite elements (corresponding to a P_2 - P_0 - P_0 discretization in the linear case) for the anisotropic wall models. We solve the monolithic system containing the fluid, the solid, and the geometry, using matching nodes at the fluid-structure interface. As in [6], a convective explicit (CE) approach is used, resulting in stronger limits for the size of the time steps than a fully implicit method. We have also implemented a fully implicit scheme. Here, we are, however, interested in the influence of the material response rather than the numerics and the performance.

We use the LifeV software library [1], based on Trilinos [24], coupled to the Finite Element Analysis Program (FEAP 8.2); cf. for a description for the lightweight interface coupling both software packages [19,22]. Following [6, section 4.2], we use a smooth ramp to apply an interior blood pressure of 80 mmHg to initiate the necessary prestretch of the arterial wall before the start of the heart beat. Using a smooth ramp can reduce unwanted oscillations by an order of magnitude; see, e.g., [7, section 4.2.2].

4.1 Flow rate, lumen area, and pressure at the in- and outflow

Neo-Hooke models NH₁ and NH₂ Our simulations show several difficulties with the Neo-Hooke parameter sets NH₁ and NH₂; see Figure 4.2. First, we observe that the sets NH₁ and NH₂ result in a material behavior, which is significantly softer than the other models: for NH₁ and NH₂, already briefly after the ramp phase (which ends at $t = 0.1$ s), the outflow areas are significantly larger than the maximum outflow area during the heart beat in the benchmark [6]; see Figure 4.2. Second, for both data sets, the computations fail near the end of the ramp shortly after strong oscillations are visible in the outflow pressure and flow rate. We believe that this is a result of wave reflections at the outflow: for NH₁ and NH₂ the absorbing boundary condition, using the parameters described in section 3.2, does not work well enough.

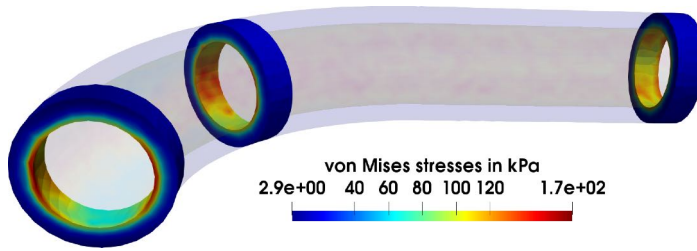


Fig. 4.1 Von Mises stresses for Ψ_A at time $t = 0.536$ s.

However, it is already clear from the ramp phase that NH_1 and NH_2 will result in in- and outflow areas, which are larger than the ones for the sophisticated models; see Figure 4.2. We will therefore consider the parameter sets NH_3 and NH_4 in section 4.1 for the comparison in the heart beat phase.

Sophisticated arterial wall models Results for the sophisticated wall models are compared in Figure 4.3. It is interesting that the in- and outflow areas are significantly larger for Ψ_A than for Ψ_B and Ψ_E . The results for Ψ_A , however, match those computed earlier in the benchmark [6]. Consulting the data fits in Figure 2.1 (or [10, Figure 2]), we observe that the curves for Ψ_B and Ψ_E seem to be quite similar, whereas the curves for Ψ_A have a slightly different shape: the curve for Ψ_A , for the circumferential direction, is steeper for large stretches than for the other models. This is especially visible for $\Delta l/l_0 > 0.25$. On the other hand, it is below the curves of Ψ_B and Ψ_E for $\Delta l/l_0 \approx 0.225$.

Considering the numerical values of the parameters (see Table 2.2), let us note that for Ψ_A the exponent ε_2 is smaller than for the other two models while the multiplicative constants c_1 and ε_2 are larger.

Note that one may be tempted to compute an (average) circumferential stretch, for instance, at the outflow from the increase in area. For Ψ_A , the increase in area from 0.070 cm to almost 0.093 cm, visible in Figure 4.3, corresponds to an (average) circumferential stretch of only about 1.15 or an increase of 15 percent. For an adequate analysis of the stress-strain response, this value is, however, misleading since the stress (and the stretch) is far from homogeneous along the circumferential and radial direction; see Figures 4.1, 4.7 and 4.9. The stresses in the wall are also concentrated at the interior of the wall, that is, at the interface to the fluid; see Figures 4.7 and 4.9.

This result may also seem surprising, since the earlier quasistatic computations in [10] indicate a smaller lumen for Ψ_A than for the other models. However, in [10] a higher internal blood pressure of 24 kPa (≈ 180 mmHg) was simulated, and a plaque was present in the lumen. Indeed, the larger lumen observed in [10] seems to be due to localized stretch near the plaque; see [10, Figures 7 to 11]; also note that the thickness of the model was only 2 mm in [10, Figures 7 to 11].

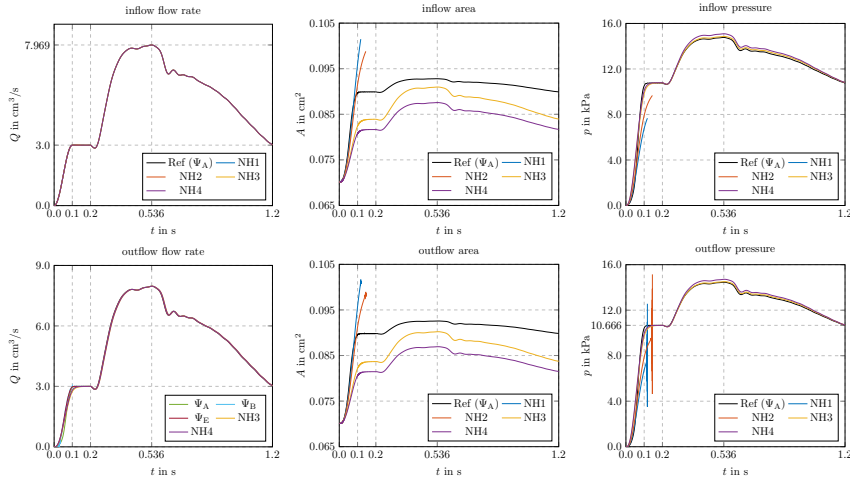


Fig. 4.2 Flow rate, area, and pressure at the inflow and the outflow for Neo-Hooke using different parameter sets.

We also observe that the results in Figure 4.2 are quite similar for Ψ_B and Ψ_E in terms of flow rate, pressure, and lumen area. However, for Ψ_B small oscillations are visible during the ramp phase; see Figure 4.3 for $0 < t < 0.2$ s and the zoom into the same data in Figure 4.4. The oscillations then vanish during the heart beat. However, since the ramp phase is only used to introduce the prestretch, we still consider this a valid simulation, despite the visible oscillations.

Heart beat phase using the sophisticated wall models and the Neo-Hooke models NH_3 and NH_4 We have also created two parameter sets for Neo-Hooke, NH_3 and NH_4 which show a similar in- and outflow area as the Ψ_* models; see Figure 4.2. The sets NH_3 and NH_4 were chosen such that they have, at the end of the ramp, a similar in- and outflow lumen area as the models Ψ_B and Ψ_E ; see Figure 4.3. The set NH_3 is slightly softer, the set NH_4 is slightly stiffer. For both Neo-Hooke sets the lumen area is slightly smaller than for Ψ_A ; see Figure 4.2.

It is clear from our simulations that the amplitude of the lumen area is much larger in NH_3 and NH_4 than in all other Ψ_* models; see Figure 4.3. This is, presumably, due to lack of fiber stiffening, which is present in the Ψ_* models. This is also a clear indication that high stresses are present, locally, in the simulations with the Ψ_* models.

Only relatively small differences between the models are visible in the flow rate and pressure.

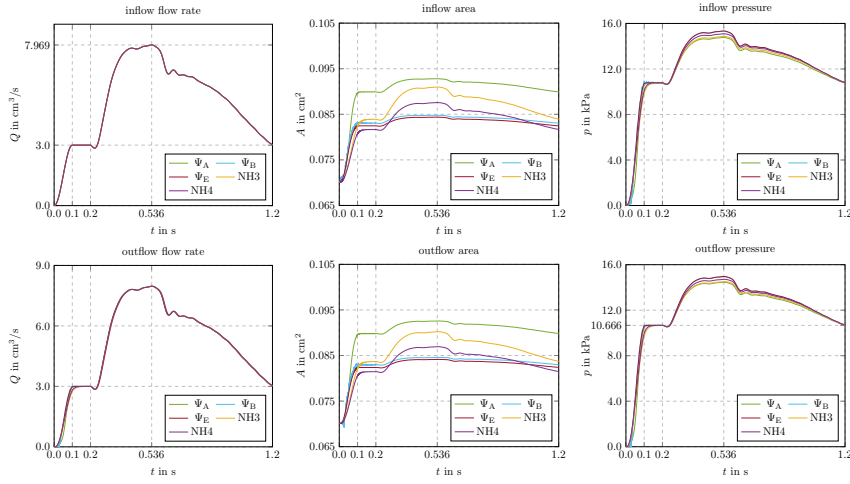


Fig. 4.3 Flow rate, area, and pressure at the inflow and the outflow for the different material models Ψ_A (parameter set 2) [8] to Ψ_E [27] and, additionally, for two Neo-Hooke (NH3 and NH4) parameter sets. The time interval $t = 0$ s to $t = 0.1$ s is the smooth ramp which introduces the prestretch, the heartbeat starts at $t = 0.2$ s. We see significant differences between the Ψ_* models and the Neo-Hooke model with respect to the outflow area: for NH3 and NH4 the outflow area has a significantly larger amplitude during the heart beat, presumably, since the model lacks fiber stiffening. Interestingly, Ψ_A (with parameter set 2) yields a significantly larger outflow area than the other Ψ_* models.

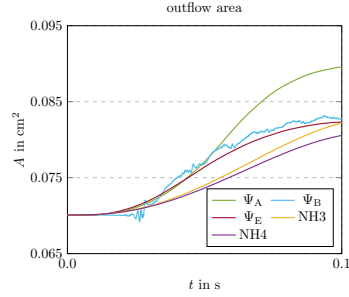


Fig. 4.4 Numerical instabilities are visible for Ψ_B during the ramp phase; cf. Figure 4.3 for the full plot.

4.2 Comparison of displacements

In Figures 4.5 and 4.6, the displacement of the structure is depicted at $t = 0.2$ s and $t = 0.536$ s, respectively. Significant differences are visible in the displacement.

While differences between the two Neo-Hooke models NH₃ and the stiffer NH₄ are visible, these differences are small compared to the sophisticated

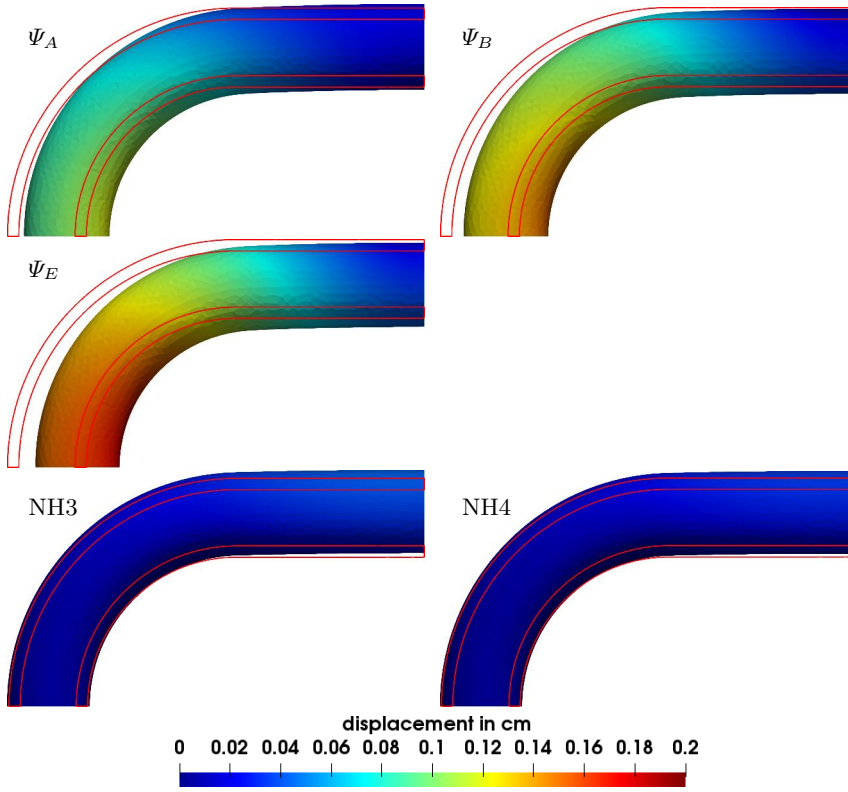


Fig. 4.5 Displacement of the arterial wall for Ψ_A , Ψ_B , Ψ_E , NH₃, and NH₄ at $t = 0.2$ s.

models Ψ_A , Ψ_B , and Ψ_E . First, the displacements for the Neo-Hooke models are significantly smaller for $t = 0.2$ s as well as for $t = 0.536$ s. Second, the tube bends outwards for the Neo-Hooke models, whereas it bends inwards for the Ψ_* models. We see from these results that, when the Neo-Hooke material model is used with parameters which result in a similar lumen area then the structure is significantly stiffer than in the other models. Lacking the terms for the stiffening fibers the Neo-Hooke model shows a completely different qualitative behavior than the other models.

When comparing the models Ψ_A , Ψ_B , and Ψ_E , it is striking that the displacement is smaller in Ψ_A than in the other Ψ_* models and that the displacement is higher in the Ψ_E model than in the other models. Note that in section 4.1, Ψ_A showed a larger lumen area than the other Ψ_* models.

4.3 Comparison of the stresses

When comparing the stresses of the different material models and parameter sets, all Ψ_* models show a very similar stress distribution; see Figure 4.7

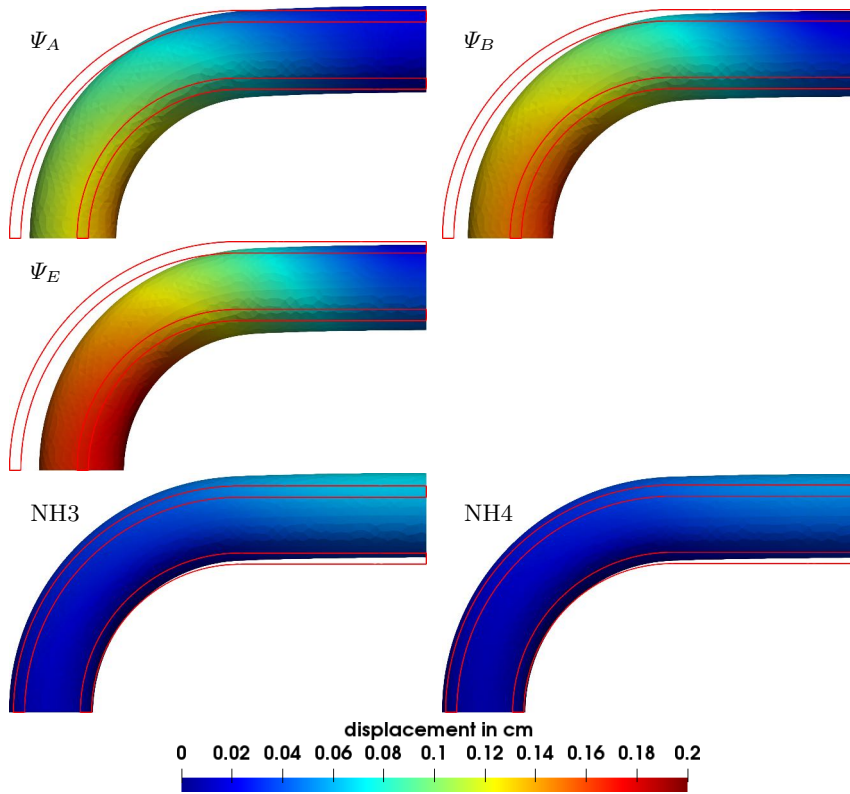


Fig. 4.6 Displacement of the arterial wall for Φ_A , Φ_B , Φ_E , NH₃, and NH₄ at $t = 0.536$ s.

for $t = 0.2$ s and Figure 4.9 for $t = 0.536$ s. All models show a very strong concentration of the stresses at the lumen interface and very low stresses at the outside of the tube.

The stress distributions of the Neo-Hooke models is, however, significantly different. The stresses are less localized at the lumen interface, instead significant stresses are visible in the complete cross section of the tube. Both observations are valid at $t = 0.2$ s as well as at $t = 0.536$ s.

4.4 Linear elastic wall models

We have also performed simulations using a linear elastic wall model. It is clear that a good fit of a linear elastic model to the experimental data cannot be achieved since the strongly nonlinear response of the wall cannot be reproduced; cf. Figure 2.1. Furthermore, if the geometrically linearized setting is considered, the solution of mechanical equilibrium equations in the undeformed configuration may not match well with the large deformations

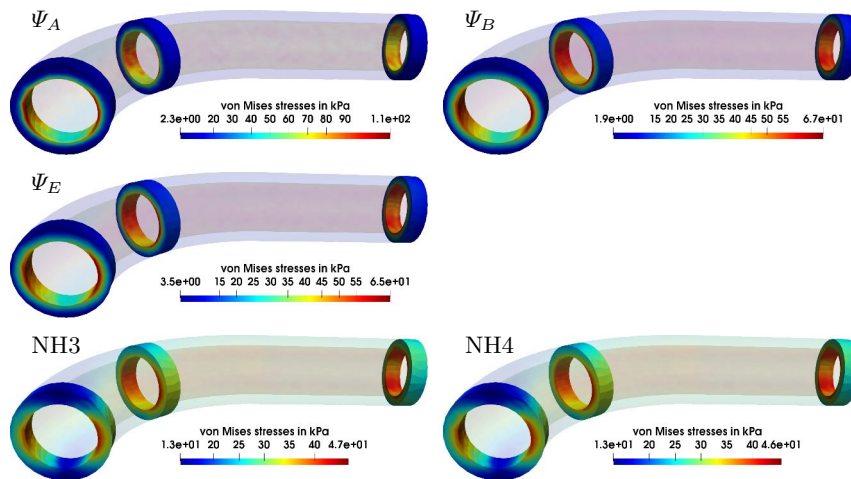


Fig. 4.7 Visualization of the von Mises stresses at $t = 0.2$ s.

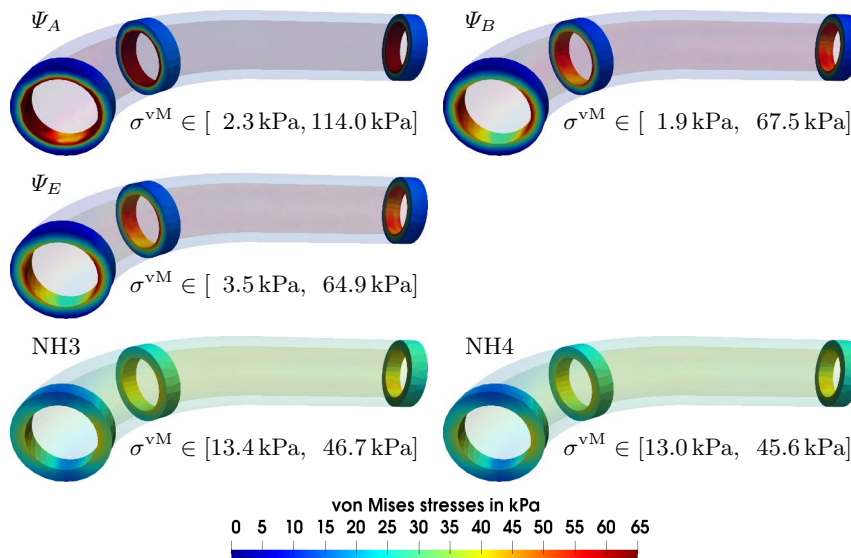


Fig. 4.8 Visualization of the von Mises stresses at $t = 0.2$ s (uses the scale of Ψ_E); see Figure 4.7 for the respective results with individual color scales.

appearing in the artery. However, the aim of this analysis is to highlight the unphysical (pathological) behavior when using linear models. To avoid an analysis, where a potentially good-natured problem is considered accidentally, we have performed a large number of simulations using 15 different linear elastic parameter sets; see Figure 4.11, where we also have provided

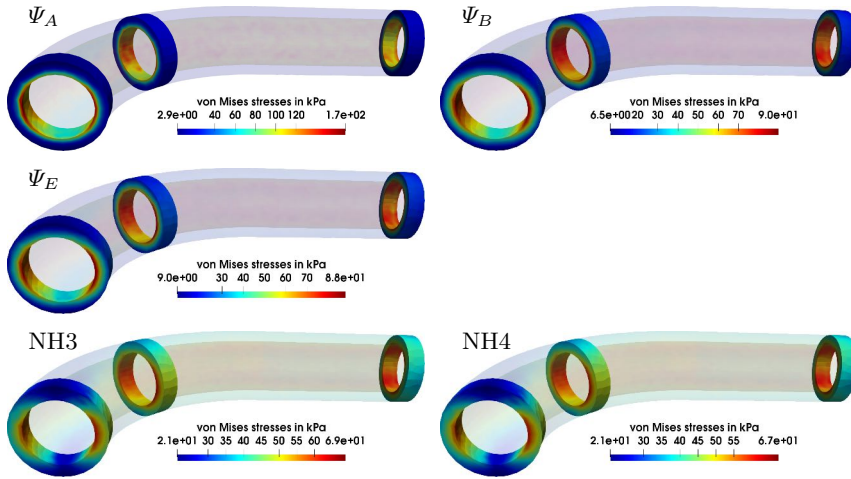


Fig. 4.9 Visualization of the von Mises stresses at $t = 0.536$.

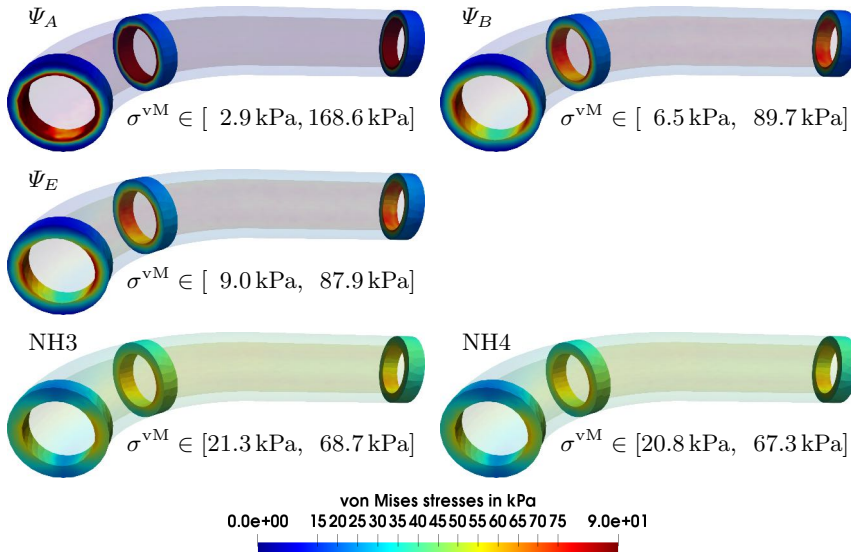


Fig. 4.10 Visualization of the von Mises stresses at $t = 0.536$ s (uses the scale of Ψ_E); see Figure 4.9 for the respective results with individual color scales.

Ψ_A as a reference. The set LE_n refers to $E = n \cdot 1000000 \text{ dyn/cm}^2$ and $\nu = 0.49$, which corresponds to a slightly compressible material.

We observe in Figure 4.11 that the softest parameter set (LE1) is quite close to the reference model Ψ_A in the time interval $0 \text{ s} < t < 0.05 \text{ s}$ with respect to the inflow and outflow areas as well as for the inflow and outflow pressures. Of course, in this time interval less than half of the stretch

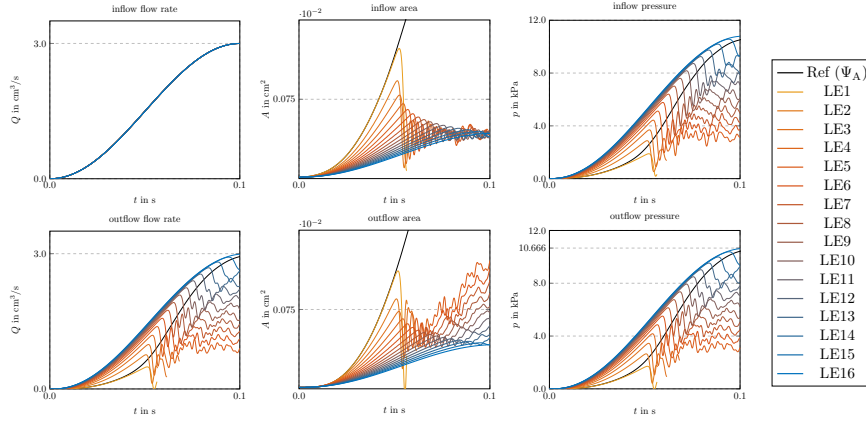


Fig. 4.11 Flow rate, area, and pressure at the inflow and the outflow for linear elasticity using different parameter sets, where LE1 exhibits the softest and LE15 the stiffest behavior.

in the inflow and outflow areas has occurred. However, briefly after 0.05 s, oscillations are visible and the simulation fails. Using stiffer parameter sets (LE2, . . . , LE14), the oscillations occur later, however, the inflow and outflow area as well as the pressure move further away from the reference Ψ_A . Only for LE15 unphysical oscillations in the simulation are avoided.

It can be assumed that the onset of the oscillations and the subsequent failure of the simulations for LE1 to LE14 are at least partially due to our boundary conditions; see section 3.2. In particular, the absorbing boundary condition may not be effective enough to remove wave reflections at the outflow for these parameter sets and the scarce boundary conditions for the structure may be prone to amplify oscillations, especially for soft wall models.

The stiffest parameter set LE15 avoids any visible oscillations for $0 \text{ s} < t < 0.1 \text{ s}$, however, the behavior in the simulation of the ramp phase is clearly too stiff if compared to the reference model Ψ_A : the inflow and outflow areas are significantly too small at $t = 0.1 \text{ s}$. However, the inflow and outflow pressures are quite close to the reference for $t = 0.1 \text{ s}$.

Despite the oscillations in the ramp phase, we have also computed the heart beat phase with the linear elastic models which did not fail. Here, we observe very large displacements which clearly seem unphysical; see Figure 4.12 for LE₅ at $t = 0.13 \text{ s}$. From the large displacements we conclude that, during the heart beat, LE₅ seems to be significantly too soft, if compared to the reference. On the other hand, it is clearly visible that, during the ramp phase, it is too stiff, compared to the reference.

We can conclude that using linear elastic wall models, using our setup, we were not successful in achieving a good agreement with the nonlinear reference.

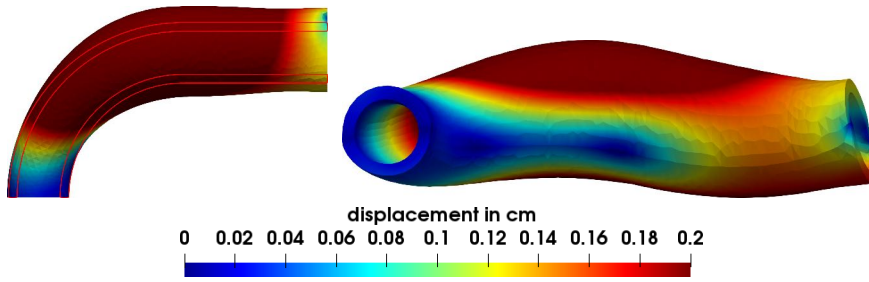


Fig. 4.12 Displacement of the arterial wall for LE5 at 0.13s.

4.5 Numerical properties of the nonlinear wall models

The numerical properties of the wall models are not identical. It is interesting that, although the results in Figure 4.3 are quite similar for Ψ_B and Ψ_E , numerically, their performance is quite different.

In Figure 4.13, we present the time steps used in the simulation, and in Figure 4.14, we compare the Newton steps needed for each second of simulation time. In Figure 4.15, we compare the number of GMRES iterations needed for each second of simulation time.

For the time stepping, we chose an initial time step of 10^{-4} which was increased to 10^{-3} and $t = 0.2$ s. However, we have observed, that for Ψ_B , initially, for $0 < t < 0.1$ s, five times smaller time steps were needed to achieve convergence; note that the time steps size has been adjusted manually until convergence could be achieved. As a consequence, also the number of Newton iterations and the number of GMRES iterations for each second of simulation time is larger for $0 < t < 0.1$ s; see Figures 4.14 and 4.15. However, we see that also for $t > 0.1$ s the computational cost remains higher for Ψ_B than for all other models: in Figure 4.15, Ψ_B needs, on average, the largest number of GMRES iterations, which indicates worse numerical properties of the linearized systems.

We also see that the computational cost in terms of iteration numbers is significantly smaller for the Neo-Hooke models compared to Ψ_A , Ψ_B , and Ψ_E : for example, for $t > 0.2$ s the number of GMRES iterations for each second of simulation time is smaller by almost a factor of two or more for the Neo-Hooke models.

Among the Ψ_* models, the model Ψ_A needs the lowest number of GMRES iterations for each second of simulation time although the difference to Ψ_E is small.

5 Conclusion

We have performed and analyzed monolithic fluid-structure interaction simulations in a curved tube benchmark geometry using three different sophisticated hyperelastic material models developed for arterial walls which have

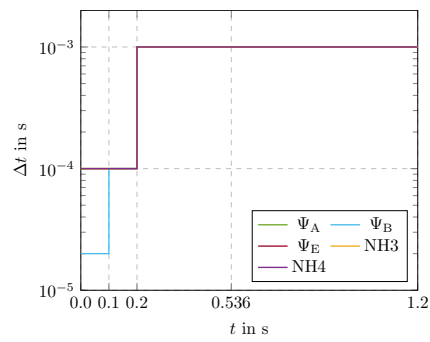


Fig. 4.13 Time step sizes used in the simulations. For Ψ_B , initially, smaller time steps are needed.

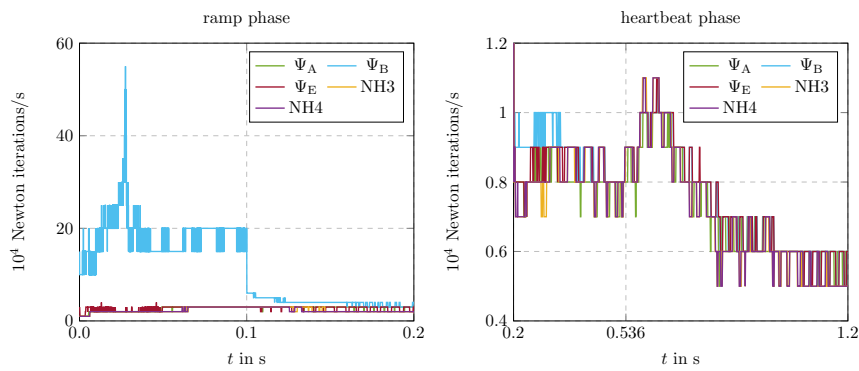


Fig. 4.14 Newton iteration counts for each second of simulation time for the different models. Initially, for $0\text{ s} < t < 0.1\text{ s}$, significantly more Newton iterations are needed for Ψ_B for each second of simulation time.

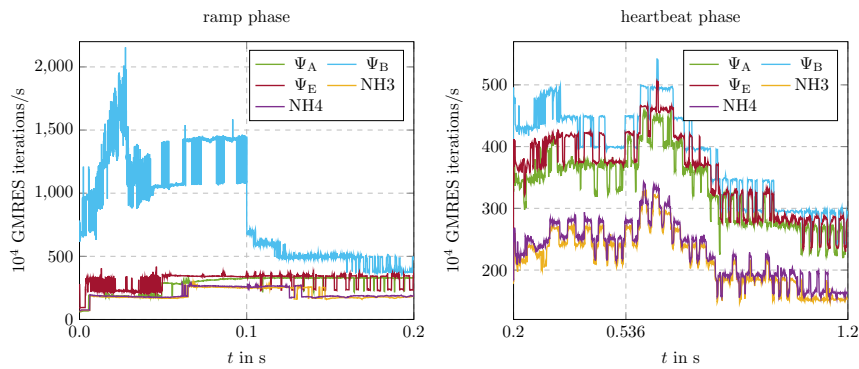


Fig. 4.15 Krylov iteration counts for each second of simulation time. Initially, significantly more GMRES iterations are needed for Ψ_B .

been successfully fitted to experimental data. These models account for the almost incompressibility of biological soft tissue as well as for the anisotropy from collagen fiber stiffening in arterial walls. We have also performed simulations using a simple Neo-Hooke model for the wall using four different parameter sets. We have found that the three sophisticated hyperelastic models showed a qualitatively similar behavior. Using the Neo-Hooke hyperelastic energy the results turned out to be different, even qualitatively. Additional simulations using the geometrically linearized setting and a linear elastic material model have shown significant numerical issues and a non-realistic qualitative and quantitative response in the considered benchmark problem. With view to the numerical performance, two of the anisotropic models from [8] and [27] have shown good properties, whereas the model based on the well-known anisotropic function [26] required a significantly larger number of Newton and GMRES iterations. Apparently, a purely isochoric, anisotropic strain energy density poses a challenge with respect to the numerical computation. Summarizing, several material models which show a quite comparable stress-strain response under uniaxial tension in circumferential- and axial direction, will not automatically lead to comparable results in simulations of arterial walls. Thereby, the results show that the decision for a particular material model should be made carefully and appears not to be a black box task.

6 Appendix: Monolithic Algorithm for Fluid-Structure Interaction

After discretization in space and time, the fully coupled nonlinear FSI system given by

$$\begin{pmatrix} F(\mathbf{u}_f^{n+1}, p^{n+1}, \mathbf{d}_f^{n+1}) + 0 & + C_1^T \boldsymbol{\lambda}^{n+1} + 0 \\ 0 & + S(\mathbf{d}_s^{n+1}) + C_3^T \boldsymbol{\lambda}^{n+1} + 0 \\ C_1 \mathbf{u}_f^{n+1} & + C_2 \mathbf{d}_s^{n+1} + 0 & + 0 \\ 0 & + C_4 \mathbf{d}_s^{n+1} + 0 & + H \mathbf{d}_f^{n+1} \end{pmatrix} = \begin{pmatrix} \mathbf{b}_f \\ \mathbf{b}_s \\ C_2 \mathbf{d}_s^n \\ 0 \end{pmatrix}. \quad (6.1)$$

Here, $\boldsymbol{\lambda}$ is the vector of Lagrange multipliers which are used to enforce the balance of normal stresses across Γ . Let us note that the fluid subproblem F and the solid subproblem S are nonlinear (unless a linear elastic wall model is used), whereas the geometry subproblem H is linear. The matrices C_1 and C_2 are used to enforce the continuity of the velocity on Γ , the transposed matrices C_1^T and C_3^T account for the balance of normal stresses, while C_4 accounts for the geometric adherence. In the case of conforming meshes and conforming discretizations at the fluid-structure interface, we have $C_1|_\Gamma = I|_\Gamma, C_3|_\Gamma = -I|_\Gamma, C_2|_\Gamma = 1/\Delta t C_3, C_4|_\Gamma = I|_\Gamma$, where $I|_\Gamma$ is the identity matrix defined on the interface Γ . For details on the fluid-structure interaction, see [6].

Acknowledgments

We would like to thank Dominik Brands, Institute of Mechanics, University of Duisburg-Essen, for fitting the Neo-Hooke models to the experimental data.

The authors Balzani, Klawonn, Rheinbach, and Schröder acknowledge funding from the “Deutsche Forschungsgemeinschaft” (DFG) under project number 214421492. The authors Balzani, Klawonn, and Rheinbach also acknowledge funding from the “Deutsche Forschungsgemeinschaft” (DFG) under project number 465228106.

The authors gratefully acknowledge the computing time granted by the Center for Computational Sciences and Simulation (CCSS) of the Universität of Duisburg-Essen and provided on the supercomputer magnetUDE (DFG Projects 263348352 and 318601939 / grants INST 20876/209-1 FUGG, INST 20876/243-1 FUGG) at the Zentrum für Informations- und Mediene Dienste (ZIM). The fourth author acknowledges computing time on the Compute Cluster of the Fakultät für Mathematik und Informatik of Technische Universität Freiberg DFG project number 397252409, operated by the university computing center URZ.

References

1. <https://bitbucket.org/lifev-dev/lifev-release/wiki/Home>.
2. J. Ball. Convexity conditions and existence theorems in non-linear elasticity. *Arch. Ration. Mech. Anal.*, 63:337–403, 1977.
3. D. Balzani, D. Böse, D. Brands, R. Erbel, A. Klawonn, O. Rheinbach, and J. Schröder. Parallel simulation of patient-specific atherosclerotic arteries for the enhancement of intravascular ultrasound diagnostics. *Engineering Computations*, 29(8):888–906, 2012.
4. D. Balzani, D. Böse, D. Brands, R. Erbel, A. Klawonn, O. Rheinbach, and J. Schröder. Parallel simulation of patient-specific atherosclerotic arteries for the enhancement of intravascular ultrasound diagnostics. *Engineering Computations*, 29(8), 2012.
5. D. Balzani, S. Brinkhues, and G. Holzapfel. Constitutive framework for the modeling of damage in collagenous soft tissues with application to arterial walls. *Computer Methods in Applied Mechanics and Engineering*, 213–216:139–151, 2012.
6. D. Balzani, S. Deparis, S. Fausten, D. Forti, A. Heinlein, A. Klawonn, A. Quarteroni, O. Rheinbach, and J. Schröder. Numerical modeling of fluid–structure interaction in arteries with anisotropic polyconvex hyperelastic and anisotropic viscoelastic material models at finite strains. *Internat. J. Numer. Methods in Biomed. Engrg*, 32(10):e02756–n/a, 2016. <http://dx.doi.org/10.1002/cnm.2756> Also Preprint 03/2015 at <http://tu-freiberg.de/fakult1/forschung/preprints>.
7. D. Balzani, S. Deparis, S. Fausten, D. Forti, A. Heinlein, A. Klawonn, A. Quarteroni, O. Rheinbach, and J. Schröder. Aspects of arterial wall simulations: Nonlinear anisotropic material models and fluid structure interaction. page 12 p., 01 2014. Proceedings of the WCCM XI.

8. D. Balzani, P. Neff, J. Schröder, and G. A. Holzapfel. A polyconvex framework for soft biological tissues. Adjustment to experimental data. *Internat. J. Solids Structures*, 43(20):6052–6070, 2006.
9. D. Balzani and M. Ortiz. Relaxed incremental variational formulation for damage at large strains with application to fiber-reinforced materials and materials with truss-like microstructures. *Computer Methods in Applied Mechanics and Engineering*, 92:551–570, 2012.
10. D. Brands, A. Klawonn, O. Rheinbach, and J. Schröder. Modelling and convergence in arterial wall simulations using a parallel FETI solution strategy. *Comput. Methods Biomech. Biomed. Engin.*, 11:569–583, 2008.
11. S. Brinkhues, A. Klawonn, O. Rheinbach, and J. Schröder. Augmented lagrange methods for quasi-incompressible materials-applications to soft biological tissue. *Internat. J. Numer. Methods Biomed. Engrg*, 29(3):332–350, 2013.
12. A. Cetin and M. Sahin. A monolithic fluid-structure interaction framework applied to red blood cells. *International Journal for Numerical Methods in Biomedical Engineering*, 35(2):e3171, 2019. e3171 cnm.3171.
13. P. Crosetto, S. Deparis, G. Fourestey, and A. Quarteroni. Parallel algorithms for fluid-structure interaction problems in haemodynamics. *SIAM J. Sci. Comput.*, 33(4):1598–1622, 2011.
14. P. Crosetto, S. Deparis, G. Fourestey, and A. Quarteroni. Parallel algorithms for fluid-structure interaction problems in haemodynamics. *SIAM J. Sci. Comput.*, 33(4):1598–1622, 2011.
15. S. Deparis, M. Discacciati, G. Fourestey, and A. Quarteroni. Fluid–structure algorithms based on steklov–poincaré operators. *Computer Methods in Applied Mechanics and Engineering*, 195(41):5797 – 5812, 2006. John H. Argyris Memorial Issue. Part II.
16. S. Deparis, D. Forti, G. Grandperrin, and A. Quarteroni. Facsi: A block parallel preconditioner for fluid–structure interaction in hemodynamics. *Journal of Computational Physics*, 327:700 – 718, 2016.
17. S. Deparis, D. Forti, A. Heinlein, A. Klawonn, A. Quarteroni, and O. Rheinbach. A comparison of preconditioners for the Steklov-Poincaré formulation of the fluid-structure coupling in hemodynamics. *PAMM*, 15(1):93–94, 2015.
18. L. Failer, P. Minakowski, and T. Richter. On the impact of fluid structure interaction in blood flow simulations. *Vietnam Journal of Mathematics*, Jan 2021.
19. A. Fischle, A. Heinlein, A. Klawonn, and O. Rheinbach. Lightweight coupling library for FEAP and LifeV. 2014.
20. D. Forti, M. Bukac, A. Quaini, S. Canic, and S. Deparis. A monolithic approach to fluid-composite structure interaction. *J. Sci. Comput.*, 72(1):396–421, 2017.
21. S. Gong and X.-C. Cai. A nonlinear elimination preconditioned inexact newton method for heterogeneous hyperelasticity. *SIAM Journal on Scientific Computing*, 41(5):S390–S408, 2019.
22. A. Heinlein. *Parallel Overlapping Schwarz Preconditioners and Multiscale Discretizations with Applications to Fluid-Structure Interaction and Highly Heterogeneous Problems*. Phd thesis, University of Cologne, 2016.
23. A. Heinlein, A. Klawonn, and O. Rheinbach. A parallel implementation of a two-level overlapping schwarz method with energy-minimizing coarse space based on trilinos. *SIAM Journal on Scientific Computing*, 38(6):C713–

- C747, 2016. Also Preprint 04/2016 on <http://tu-freiberg.de/fakult1/forschung/preprints>.
24. M. A. Heroux, R. A. Bartlett, V. E. Howle, R. J. Hoekstra, J. J. Hu, T. G. Kolda, R. B. Lehoucq, K. R. Long, R. P. Pawlowski, E. T. Phipps, A. G. Salinger, H. K. Thornquist, R. S. Tuminaro, J. M. Willenbring, A. Williams, and K. S. Stanley. An overview of the Trilinos project. *ACM Trans. Math. Softw.*, 31(3):397–423, 2005.
 25. G. Holzapfel. Determination of material models for arterial walls from uniaxial extension tests and histological structure. *Journal of Theoretical Biology*, 238(2):290–302, 2006.
 26. G. Holzapfel, T. Gasser, and R. Ogden. A new constitutive framework for arterial wall mechanics and a comparative study of material models. *Journal of Elasticity*, 61:1–48, 2000.
 27. G. Holzapfel, T. Gasser, and R. Ogden. Comparison of a multi-layer structural model for arterial walls with a fung-type model, and issues of material stability. *Journal of Biomechanical Engineering*, 126:264–275, 2004.
 28. D. Jodlbauer, U. Langer, and T. Wick. Parallel block-preconditioned monolithic solvers for fluid-structure interaction problems. *International Journal for Numerical Methods in Engineering*, 117(6):623–643, 2019.
 29. F. Kong and X.-C. Cai. Scalability study of an implicit solver for coupled fluid-structure interaction problems on unstructured meshes in 3d. *International Journal of High Performance Computing Applications*, 32, 05 2016.
 30. F. Kong, V. Kheyfets, E. Finol, and X.-C. Cai. An efficient parallel simulation of unsteady blood flows in patient-specific pulmonary artery. *International journal for numerical methods in biomedical engineering*, 34, 12 2017.
 31. M. Motevalli, J. Uhlemann, N. Stranghöner, and D. Balzani. Geometrically nonlinear simulation of textile membrane structures based on orthotropic hyperelastic energy functions. *Composite Structures*, 223:110908, 2019.
 32. F. Nobile and C. Vergara. An effective fluid-structure interaction formulation for vascular dynamics by generalized robin conditions. *SIAM Journal on Scientific Computing*, 30(2):731–763, 2007. cited By 112.
 33. M. Razzaq, H. Damanik, J. Hron, A. Ouazzi, and S. Turek. Fem multigrid techniques for fluid–structure interaction with application to hemodynamics. *Applied Numerical Mathematics*, 62(9):1156 – 1170, 2012. Numerical Analysis and Scientific Computation with Applications (NASCA).
 34. J. Schröder and P. Neff. Invariant formulation of hyperelastic transverse isotropy based on polyconvex free energy functions. *International Journal of Solids and Structures*, 40:401–445, 2003.
 35. J. Schröder, P. Neff, and D. Balzani. A variational approach for materially stable anisotropic hyperelasticity. *International Journal of Solids and Structures*, 42(15):4352–4371, 2005.
 36. A. Spencer. Isotropic polynomial invariants and tensor functions. In J. Boehler, editor, *Applications of Tensor Functions in Solid Mechanics*, number 292 in CISM Course. Springer, San Francisco, CA, 1987.
 37. S. Turek, J. Hron, M. Mádlík, M. Razzaq, H. Wobker, and J. F. Acker. Numerical simulation and benchmarking of a monolithic multigrid solver for fluid-structure interaction problems with application to hemodynamics. In H.-J. Bungartz, M. Mehl, and M. Schäfer, editors, *Fluid Structure Interaction II*, pages 193–220, Berlin, Heidelberg, 2010. Springer Berlin Heidelberg.